

# Floquet scattering of light and sound in Dirac optomechanics

C. Wurl\* and H. Fehske†

*Institut für Physik, Universität Greifswald, 17487 Greifswald, Germany*

(Dated: April 21, 2022)

The inelastic scattering and conversion process between photons and phonons by laser-driven quantum dots is analyzed for a honeycomb array of optomechanical cells. Using Floquet theory for an effective two-level system, we solve the related time-dependent scattering problem, beyond the standard rotating-wave approximation approach, for a plane Dirac-photon wave hitting a cylindrical oscillating barrier that couples the radiation field to the vibrational degrees of freedom. We demonstrate different scattering regimes and discuss the formation of polaritonic quasiparticles. We show that sideband-scattering becomes important when the energies of the sidebands are located in the vicinity of avoided crossings of the quasienergy bands. The interference of Floquet states belonging to different sidebands causes a mixing of long-wavelength (quantum) and short-wavelength (quasiclassical) behavior, making it possible to use the oscillating quantum dot as a kind of transistor for light and sound. We comment under which conditions the setup can be utilized to observe *zitterbewegung*.

## I. INTRODUCTION

Optomechanical systems realizing the interaction between light and matter on the micro- and macroscale [1], enjoy continued interest since they allow for the study of fundamental questions concerning, e.g., the cooling of nanomechanical oscillators into the quantum ground-state [2–4], nonlinear phenomena on the route from classical [5, 6] to quantum behavior [7–9], and even entanglement [10, 11] and (quantum) information processing [12–15]. Regarding the latter one, optomechanical crystals or arrays [16–19] have gained particular attention as they accommodate (strongly) coupled collective modes [20–22], and therefore can be utilized for the transport, storage and transduction of photons and phonons [23–27].

A promising building block for hybrid photon-phonon signal processing architectures is provided by planar optomechanical metamaterials. Their optically tunable, polariton-like bandstructure enables versatile and easy to implement applications of artificial optomechanical gauge fields [28–30] and topological phases of light and sound [31]. In this context, the emergence of Dirac physics was demonstrated for low-energy photons and phonons in ‘optomechanical graphene’, that is a honeycomb array of optomechanical cells [32]. In these systems ultrarelativistic transport phenomena such as Klein-tunneling appear, because of the chiral nature of the quasiparticles and their Dirac-like bandstructure, just as for Dirac-electrons in graphene. Moreover, the radiation pressure that induces the coupling between photons and phonons inside the optomechanical barrier can be easily tuned by the laser power and may cause the formation of (photon-phonon) polariton states mixing photonic and phononic contribution. This leads to new transport phenomena such as the interconversion

between light and sound. Circular barriers are of special interest because they are easier to implement experimentally than infinite planar barriers and show a richer scattering behavior due to their finite size. In particular such ‘quantum dots’ may cause the spatial and temporal trapping, Veselago lensing, a depletion of Klein-tunneling, and angle-dependent interconversion of photons and phonons [33].

Since transport of Dirac-quasiparticles is extremely energy-sensitive, external time-dependent fields may produce interesting effects. This has been demonstrated for the photon-assisted transport in graphene-based nanostructures [34], where planar and circular electromagnetic potentials, oscillating with frequency  $\Omega$ , give rise to inelastic scattering processes by exchanging energy quanta  $n\hbar\Omega$  with the oscillating field. Thereby, the excitation into and interference between sideband states may cause the suppression of (Klein-) tunneling, Floquet-Fano resonances, as well as highly anisotropic angle-resolved transmission and emission of the quasiparticles [35–40]. Also the relevance to *zitterbewegung* has been addressed within the Tien-Gordon setup [41].

As stressed already, inside the optomechanical barrier polaritonic quasiparticles will form. They can be treated effectively as two-level systems. Then, modulating the coupling strength in a time-periodic way, the system mimics a two-level system driven by a linear polarized laser field. Within Floquet theory, it was shown that such systems exhibit strongly enhanced transmission probabilities between the two levels whenever avoided crossings occur in the quasienergy bands [42–44]. This immediately raises the question how Floquet-driven barriers affect the two-level scattering process in optomechanical metamaterials. For planar oscillating barriers we found that the finite transmission probabilities for the sidebands might suppress or revive the light-sound interconversion when the energy of the incident photon is close to multiples of the oscillation frequency [45].

Motivated by these findings, in the present paper we study the inelastic scattering and conversion process be-

\* wurl@physik.uni-greifswald.de

† fehske@physik.uni-greifswald.de

tween photons and phonons triggered by periodically oscillating quantum dots, imprinted optically in optomechanical graphene. Fig. 1 illustrates the setup under consideration. The paper is organized as follows. Section II presents our model and outlines the theoretical approach, based on Floquet theory for an effective two-level system. The solution of the related time-dependent scattering problem is explicitly given. A more detailed presentation of the (numerical) implementation of our Floquet approach can be found in the Appendix . In Sec. III, after briefly recapitulating previous findings for the static quantum dot, we discuss the numerical results obtained for the oscillating quantum dot in the whole range of system parameters. The relevance for observing ZB is also considered. Our main conclusions can be found in Sect. IV.

## II. THEORETICAL APPROACH

### A. Model

In optomechanical graphene, driven by a laser with frequency  $\omega_{las}$ , co-localized cavity photon (eigenfrequency  $\omega_o$ ) and phonon (eigenfrequency  $\omega_m$ ) modes interact via radiation pressure. For sufficiently low energies and barrier potentials that are smooth on the scale of the lattice constant but sharp on the scale of the de Broglie wavelength (i.e., the size of the dot is much bigger than the lattice spacing in the optomechanical array), the continuum approximation applies [46]. Then the system can be described by the optomechanical Dirac-Weyl Hamiltonian [32]

$$H = \left( \bar{v} + \frac{1}{2} \delta v \tau_z \right) \boldsymbol{\sigma} \cdot \mathbf{k} - g(\mathbf{r}, t) \tau_x. \quad (1)$$

In Eq. (1), the model Hamiltonian is written in units of  $\hbar$ , after rescaling  $H \rightarrow H - \hbar \omega_m$ . Here,  $\bar{v} = (v_o + v_m)/2$ ,  $\delta v = v_o - v_m$ , with  $v_{o/m}$  as the Fermi velocity of the optical/mechanical mode,  $\boldsymbol{\tau}$  and  $\boldsymbol{\sigma}$  are Pauli spin matrices,  $\mathbf{k}(\mathbf{r})$  gives the wavevector (position vector) of the Dirac wave, and  $g(\mathbf{r}, t)$  parametrizes the time-dependent photon-phonon coupling strength. On the other hand, when the laser continuously drives a certain region of the honeycomb lattice, a quantum barrier with time-independent coupling strength  $g_0$  is created.

We note that the above single-valley Hamiltonian is obtained after linearizing the dynamics around the steady-state solution and taking advantage of the rotating-wave approximation (RWA) in the red detuned moderate-driving regime,  $\Delta = \omega_{las} - \omega_o = -\omega_m$  [32]. To account for inelastic scattering, we assume the laser amplitude to be modulated with a frequency much smaller than the frequencies of both the laser and mechanical modes,  $\Omega \ll \omega_{las}, \omega_m$  (otherwise the RWA is not granted). Furthermore,  $\Omega$  should be much smaller than the mechanical hopping in the array, i.e.,  $\Omega < 2v_m/3a$  with  $a$  as the lattice constant (otherwise the continuum approximation is

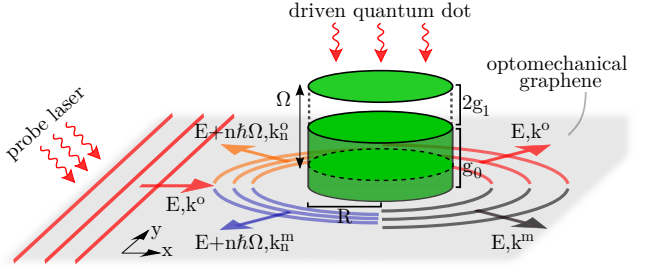


FIG. 1. (Color online) Sketch of the scattering setup. Injected by a probe laser, an incident optical wave with energy  $E > 0$  and wavevector  $\mathbf{k}^o = k^o \mathbf{e}_x$  hits a laser-driven quantum dot of radius  $R$ . Inside the dot, the photon-phonon coupling is  $g = g_0 - 2g_1 \cos(\Omega t)$ . As a result, reflected optical and mechanical waves appear with wavevectors  $\mathbf{k}^{o/m}$  ( $\mathbf{k}_{n=0} \equiv \mathbf{k}$ ), in the central band with energy  $E$ , and in the sidebands with energies  $E_n = E + n\hbar\Omega$ , where  $n = \pm 1, \pm 2, \dots$ . The reflected waves are directed away from the dot and carry an angular momentum. Since the dot allows for the conversion between light and sound, mechanical waves appear outside the dot even though the coupling vanishes here. Note that the figure is not true to scale and, since  $v_o > v_m$ , the photon/phonon wavevectors  $k_n^{o/m} = |E_n|/\hbar v_{o/m}$  are not equal in magnitude.

not granted) [32]. Then, using polar coordinates, the photon-phonon coupling in the quantum dot region with radius  $R$  takes the form

$$g(r, t) = [g_0 - 2g_1 \cos(\Omega t)] \Theta(R - r), \quad (2)$$

where  $g_0 > 0$  and  $g_1 < 0$ , and  $g_{0,1}$  are assumed to be constant. Furthermore, in order to ensure a laser amplitude greater than zero,  $2|g_1| \leq g_0$ . In what follows, for the sake of simplicity, the potential barrier (2) is assumed to be infinitely sharp. Numerical studies have shown that a more realistic steep but rounded barrier will influence the results little (due to the small Umklapp scattering) [32].

At this point we should mention that the Hamiltonian (1), derived for the linear regime within the RWA, takes into account dissipation effects in an effective way [1, 32]. Accordingly, the quasiparticles described by the model (1) propagate as undamped optical and mechanical excitations on the honeycomb lattice. As shown in Ref. [32] the main effect of dissipation would be the decay of the field amplitudes. For the same reason, the barrier is described by the optomechanical coupling strength  $g$  (being proportional to the laser amplitude) and not by the single-photon coupling rate.

Inside the quantum dot, where the photon-phonon coupling is finite, the polariton quasiparticle states are superpositions of optical and mechanical eigenstates of  $\tau_z$ . Given the time-periodic coupling (2), the polariton states can be treated as periodically driven two-level systems. A similar approach is widely used in quantum optics (Rabi model), e.g., in order to model atoms or superconducting qubits driven by a semiclassical, linearly polarized laser field (see Ref. [47] and references cited therein). There it is convenient to obtain the time-dependent so-

lutions within the rotating-wave approximation, which is justified for laser frequencies close to the transition frequency between the two energy levels of the state. In view of solving the scattering problem, however, the rotating-wave approximation cannot be applied because the wavenumber  $k$ , which enters the transition frequency between the two polariton states,  $\delta v k/2$  in (1), changes as a result of inelastic scattering processes. Therefore we make use of the Floquet formalism to find the time-dependent solutions of our scattering problem. The Floquet formalism is described, e.g., in Refs. [44, 47, 48]; for its application to two-level systems see Refs. [42, 43, 49].

## B. Formulation of the Floquet scattering problem

Treating the inelastic scattering problem we look for solutions  $|\psi(t)\rangle$  of the time-dependent Dirac equation  $i(\partial/\partial t)|\psi(t)\rangle = H|\psi(t)\rangle$ . Since the Hamiltonian is time-periodic, according to Floquet's theorem [50], we write the time-dependent solution as  $|\psi(t)\rangle = e^{-i\varepsilon t}|\varepsilon(t)\rangle$  with quasienergy  $\varepsilon$  and the time-periodic Floquet state  $|\varepsilon(t)\rangle = |\varepsilon(t+T)\rangle$ , where  $T = 2\pi/\Omega$ . For constructing the latter we use the eigensolutions in the absence of the oscillating barrier [32, 33], which are given as  $|\tau\rangle|\sigma, \mathbf{k}\rangle$ . Here,  $|\sigma, \mathbf{k}\rangle$  is the eigenvector of the single-particle Dirac-Weyl Hamiltonian  $H = \sigma \mathbf{k}$  with eigenvalue  $\sigma |\mathbf{k}|$  and sublattice pseudospin  $\sigma = \pm 1$  (in this notation  $\sigma$  acts as a band index). The polariton state is formed according to  $|\tau\rangle = \mathcal{N}^\tau(g_0|o\rangle + \gamma^\tau|m\rangle)$ , where  $\tau = \pm 1$  denotes the polariton pseudospin, and  $|o/m\rangle$  are the bare optical/mechanical eigenstates of  $\tau_z$  (the factors  $\mathcal{N}^\tau$  and  $\gamma^\tau$  are given in the Appendix). Expanding the Floquet state in a Fourier series,

$$|\varepsilon(t)\rangle = \sum_p \sum_{\tau=\pm} c_p^\tau |\tau\rangle |\sigma, \mathbf{k}\rangle e^{ip\Omega t}, \quad p \in \mathbb{Z}, \quad (3)$$

the two polariton states with  $\tau = \pm 1$  have to be superimposed because of the optomechanical coupling in  $\tau$ -space. Inserting the ansatz (3) into the time-dependent Dirac equation yields the Floquet eigenvalue equation (FEE)  $\mathcal{F}\mathbf{c} = \varepsilon\mathbf{c}$ , where  $\mathbf{c}$  is the vector containing the Fourier coefficients  $c_p^\tau$ , and  $\mathcal{F}$  is the Floquet matrix having eigenvalues  $\varepsilon$ . The Floquet matrix and the FEE in component form are given in the Appendix, see Eq. (A.5) and Eq. (A.1), respectively. In general, an analytical solution of the FEE does not exist [47]. This is in contrast to the scattering of graphene-electrons by time-periodic gate-defined potential barriers, for which the diagonal potential in sublattice space allows to integrate the Dirac equation [34, 36, 40, 41]. We therefore determine the solutions of the FEE numerically, see Appendix.

Let us take another look at the Floquet-scattering setup depicted in Fig. 1. Since the oscillating quantum dot gives (takes) energy to (away from) photons and phonons in form of multiple integers of the oscillation frequency,  $E_n = E + n\Omega$  ( $n \in \mathbb{Z}$ ), the scattering is inelastic. This implies that the wavefunctions have to be expressed

as superpositions of states with energies  $E_n$ . This is certainly unproblematic outside the dot, where the coupling is zero and we can use the unperturbed eigensolutions. The transmitted wave inside the dot, however, is composed of Floquet states according to Eq. (3). On that account the wavenumbers  $q_n^{(\pm)}$  and the Fourier coefficients  $c_{p,n}^{\tau,(\pm)}$  at each energy  $E_n = \varepsilon^{(\pm)}$  have to be determined by numerical diagonalization of the Floquet matrix  $\mathcal{F}$ . Note that the index  $(\pm)$  appears because the quasienergies are two-fold degenerate owing to the polariton pseudospin  $\tau$ .

## C. Solution of the Floquet scattering problem

For this purpose, we expand the plane wave state of the incoming photon in polar coordinates,

$$|\psi^{in}\rangle = \frac{1}{\sqrt{2}} \begin{pmatrix} 1 \\ 1 \end{pmatrix} e^{ik^o x} |o\rangle e^{-iE t} = \sum_{n,l} \delta_{no} \phi_{n,l}^{(1)}(k_n^o r) |o\rangle e^{-iE_n t}, \quad (4)$$

where  $l \in \mathbb{Z}$  is the quantum number referring to the angular momentum. The reflected (scattered) wave consists of optical and mechanical modes,  $|\psi^r\rangle = |\psi^{r;o}\rangle + |\psi^{r;m}\rangle$  (cf. Fig. 1), with

$$|\psi^{r;o/m}\rangle = \sum_{n,l} \sqrt{\frac{v_o}{v_{o/m}}} r_{n,l}^{o/m} \phi_{n,l}^{(3)}(k_n^{o/m} r) |o/m\rangle e^{-iE_n t}. \quad (5)$$

Here,  $r_{n,l}^{o/m}$  are the optical/mechanical reflection coefficients. According to Eq. (3), the transmitted wave  $|\psi^t\rangle = |\psi^{t;(+)}\rangle + |\psi^{t;(-)}\rangle$  reads

$$|\psi^{t;(\pm)}\rangle = \sum_{n,l} t_{n,l}^{(\pm)} \phi_{n,l}^{(1)}(q_n^{(\pm)} r) \times \sum_p \sum_{\tau=\pm} c_{p,n}^{\tau,(\pm)} |\tau\rangle_n^{(\pm)} e^{-iE_{n-p} t}, \quad (6)$$

where  $t_{n,l}^{(\pm)}$  are the transmission coefficients. The Fourier coefficients and wavenumbers used in Eq. (6) are extracted from the Floquet approach outlined in the Appendix. For the wavefunctions (4)-(6) we have used the eigenfunctions  $\langle \mathbf{r} | \sigma, \mathbf{k} \rangle$  of the Dirac-Weyl Hamiltonian [40, 51, 52],

$$\phi_{n,l}^{(1,3)}(k_n r) = \frac{1}{\sqrt{2}} i^{l+1} \begin{pmatrix} -i \mathcal{Z}_l^{(1,3)}(k_n r) e^{il\varphi} \\ \sigma_n \mathcal{Z}_{l+1}^{(1,3)}(k_n r) e^{i(l+1)\varphi} \end{pmatrix}, \quad (7)$$

where  $\mathcal{Z}^{(1,3)} = J_l, H_l$  denotes the Bessel/Hankel function. To ensure that the group velocity of the reflected wave is directed away from the quantum dot (as it should be for an outgoing wave), the sign of the energy determines which kind of Hankel function is used:  $H_l = J_l + i\sigma_n^{out} Y_l$  ( $Y_l$  is the Neumann function). Here,  $\sigma_n^{out} = \text{sgn}(E_n)$  is the 'band index' outside the quantum dot. Its presence in the Hankel function ensures that

the refractive indices are negative for negative energies, meaning that the wavevector is directed opposite to the propagation direction of the particle. For the transmitted wave inside the dot,  $\sigma_n^{ins} = \pm 1$  for  $E_n \gtrless \pm g_0$ , and  $\sigma_n^{ins(\pm)} = \pm 1$  for  $-g_0 \leq E_n \leq g_0$ . Matching the wave functions at  $r = R$  yields the equations for the transmission coefficients:

$$\delta_{p0} W_{p,l}^o = \sum_n \sum_{\tau=\pm} t_{n,l}^{(\tau)} f_{n-p,n}^{(\tau)} X_{n,p,l}^{o,(\tau)}, \quad (8a)$$

$$0 = \sum_n \sum_{\tau=\pm} t_{n,l}^{(\tau)} h_{n-p,n}^{(\tau)} X_{n,p,l}^{m,(\tau)}. \quad (8b)$$

The reflection coefficients can be obtained from

$$r_{p,l}^o = \sum_n \sum_{\tau=\pm} t_{n,l}^{(\tau)} f_{n-p,n}^{(\tau)} \frac{\mathcal{Z}_l^{(1)}(q_n^{(\tau)} R)}{\mathcal{Z}_l^{(3)}(k_p^o R)} - \delta_{p0} \frac{\mathcal{Z}_l^{(1)}(k_p^o R)}{\mathcal{Z}_l^{(3)}(k_p^o R)}, \quad (9a)$$

$$r_{p,l}^m = \sum_n \sum_{\tau=\pm} t_{n,l}^{(\tau)} h_{n-p,n}^{(\tau)} \frac{\mathcal{Z}_l^{(1)}(q_n^{(\tau)} R)}{\mathcal{Z}_l^{(3)}(k_p^m R)}. \quad (9b)$$

Here, we have used the abbreviations

$$W_{p,l}^o = \mathcal{Z}_l^{(1)}(k_p^o R) \mathcal{Z}_{l+1}^{(3)}(k_p^o R) - \mathcal{Z}_{l+1}^{(1)}(k_p^o R) \mathcal{Z}_l^{(3)}(k_p^o R), \quad (10a)$$

$$X_{n,p,l}^{o/m,(\tau)} = \sigma_p^{out} \mathcal{Z}_l^{(1)}(q_n^{(\tau)} R) \mathcal{Z}_{l+1}^{(3)}(k_p^{o/m} R) - \sigma_n^{ins(\tau)} \mathcal{Z}_{l+1}^{(1)}(q_n^{(\tau)} R) \mathcal{Z}_l^{(3)}(k_p^{o/m} R), \quad (10b)$$

and

$$f_{n-p,n}^{(\tau)} = \sum_{\tau'} c_{n-p,n}^{\tau',(\tau)} \mathcal{N}_n^{\tau',(\tau)} g_0, \quad (11a)$$

$$h_{n-p,n}^{(\tau)} = \sum_{\tau'} c_{n-p,n}^{\tau',(\tau)} \mathcal{N}_n^{\tau',(\tau)} \gamma_n^{\tau',(\tau)}. \quad (11b)$$

When solving the infinite-dimensional coupled linear system (8) numerically, we raise the dimension of the coefficient (scattering) matrix until convergence is reached. This is most challenging for large  $g_1$  or small  $\Omega$ , since the dimension of the scattering matrix is mainly determined by the ratio  $|g_1|/\Omega$ , cf. Appendix.

The inelastic scattering and conversion process between photons and phonons is characterized by the scattering efficiency  $Q^{o/m}(r, t)$ , that is, the scattering cross section divided by the geometric cross section. This quantity is proportional to  $(1/2R) \int j_r^{r;o/m}(r, t) r d\varphi$  [33, 40, 51, 52]. It consists of a time-averaged part

$$\bar{Q}^{o/m} = \sum_n \sum_{l=0}^{\infty} \bar{Q}_{n,l}^{o/m} = \sum_n \sum_{l=0}^{\infty} \frac{4}{k_n^{o/m} R} \left| r_{n,l}^{o/m} \right|^2, \quad (12)$$

and a time-dependent part (to simplify the notation, we omit the index  $out$  in  $\sigma_n^{out}$ )

$$\tilde{Q}^{o/m}(r, t) = \sum_{n < n'} \sum_{l=0}^{\infty} (-1)^l \frac{4}{\sqrt{k_n^{o/m} k_{n'}^{o/m}} R} \times 2\Re \left\{ (r_{n',l}^{o/m})^* r_{n,l}^{o/m} i^{\frac{1}{2}(\sigma_{n'} - \sigma_n)} e^{i(n-n')\Omega\vartheta^{o/m}} \right\}. \quad (13)$$

Here,  $\vartheta^{o/m} = r/v_{o/m} - t$  denotes the time-retarded phase factor. In Eqs. (12), (13), and hereafter,  $l \geq 0$ . The quantities  $\bar{Q}_{n,l}^{o/m}$  in Eq. (12) represent the scattering contributions of the partial wave  $l$  and the sideband  $n$ . In the far-field, the scattering efficiency is obtained from the radial component of the current density of the reflected wave,

$$j_r^{r;o/m}(r, t) = \sum_{n,n'} \sum_{l,l'} \frac{4v_o}{\pi \sqrt{k_n^{o/m} k_{n'}^{o/m} r}} (r_{n',l'}^{o/m})^* r_{n,l}^{o/m} \times i^{l-l'} i^{\frac{1}{2}(\sigma_{n'} - \sigma_n)} i^{(l+l')\text{sgn}(\sigma_{n'} - \sigma_n) + (l'-l)\text{sgn}(\sigma_{n'} + \sigma_n)} \times \{ \cos[(l+l'+1)\varphi] + \cos[(l-l')\varphi] \} e^{i(n-n')\Omega\vartheta^{o/m}}, \quad (14)$$

which characterizes the angular scattering. In the near-field, the scattering is further specified by the probability density  $\rho = \langle \psi | \psi \rangle$ , with  $|\psi\rangle = |\psi^{in}\rangle + |\psi^r\rangle$  outside and  $|\psi\rangle = |\psi^t\rangle$  inside the quantum dot. Note that in the far-field, the optical/mechanical part of the probability density of the reflected wave  $\langle \psi^r | \psi^r \rangle$  becomes equal to the current density (14) except for a constant factor  $v_{o/m}$ . Furthermore, defining the scattering efficiency by the cross section, only the incident current of the photon was used, since no phonon incident currents exist, cf. Fig. 1. Therefore, the scattering efficiency of the phonon  $Q^m$  can be understood as an interconversion rate between photons and phonons, which we can define as  $Q^m/Q^o$ .

### III. NUMERICAL RESULTS

Since the scattering problem worked out in the preceding section is invariant under the transformation  $[E, g_{0,1}, \Omega, R^{-1}] \rightarrow \gamma [E, g_{0,1}, \Omega, R^{-1}]$  with  $\gamma \in \mathbb{R}$ , we rescale the equations of motion such that  $\Omega = 1$  [45]. We set  $v_o = 10v_m$  and furthermore employ units such that  $v_o = \hbar = 1$  [32, 33, 45]. Then, the rescaled variables are dimensionless and related to the unscaled variables (marked by  $\hat{\cdot}$ ) according to  $E = \hat{E}/(\hbar\Omega)$ ,  $g_{0,1} = \hat{g}_{0,1}/\Omega$ ,  $R = \hat{R}\Omega/v_o$ ,  $k = \hat{k}v_o/\Omega$ . The phase factor is measured in units of  $\Omega$ ,  $\vartheta^{o/m} = \hat{\vartheta}^{o/m}\Omega$ . According to the experimental parameters given in Ref. [17] the effects discussed in this paper should be observable for oscillation frequencies  $\hat{\Omega} \sim 0.5\text{MHz} \ll \omega_{las}$ , where we have assumed a laser-enhanced optomechanical coupling strength  $\hat{g}_0 \sim 0.1\text{MHz}$  with  $2|\hat{g}_1| \lesssim \hat{g}_0$ . Then, without violating the continuum approximation, the energies of the photon and the phonon are in the order of  $\hbar\omega_m$  (microwaves) with excitation energies  $n\Omega \sim \text{MHz} \ll \omega_m$  for the sidebands. The typical size of the quantum dot radius is  $100a$  with lattice constant  $a \sim 50\mu\text{m}$ . Using these parameters the photon tunneling rate  $J$  between two sites [32] has to be made small by design:  $J = 2v_o/3a \sim 10^{-2}\omega_m$ .

### A. Static quantum dot

The scattering problem of the static dot ( $g_1 = 0$ ) has been analyzed in previous work [33]. Depending of the strength parameter  $Rg_0$  and the size parameter  $ER$ , different scattering regimes occur. They can be characterized by the scattering efficiency, see Fig. 2. This schematic figure is taken as starting point, helping us to classify the different parameter regimes and expected physical phenomena in the theoretical discussion below.

Comparing the scattering regimes of our optomechanical quantum dot (Fig. 2) with those of electrons in graphene scattered by gate-defined quantum dots (cf. Fig. 3 in Ref. [53]), strong similarities could be identified, which perhaps is not surprising in view of the close relation between both Hamiltonians. The most crucial difference is the non-diagonal optomechanical coupling, which allows the quantum dot to translate light into sound. The interconversion rate  $Q^m/Q^o$  is determined by the energy-coupling ratio  $E/g_0$  (see Fig. 3 in [33]) and discriminates between the optomechanical and purely optical regimes (dashed line in Fig. 2). For  $E/g_0 \ll 1$ , i.e., in the resonant scattering (quantum) regime, the size parameter is small for not too large radii ( $ER \ll 1$ ), so the excitation of the first partial waves leads to sharp resonances in the scattering efficiency of the photon, and of the phonon accordingly. The resonance condition is

$$Rg_0 = \sqrt{v_o v_m} j_{l,i}, \quad (15)$$

where  $j_{l,i}$  denotes the  $i$ 'th zero of the Bessel function  $J_l$  with  $i = 0, 1, 2, \dots$  (the onset of the resonant scattering regime is marked by an arrow in Fig. 2). Resonances are featured by quasi-bound states in the quantum dot and preferred scattering directions in the far-field (cf., Fig. 4 in [33]). Increasing  $E/g_0$  the phonon is hardly scattered and the scattering becomes weaker. In the limit  $E/g_0 \gg 1$ , the scattering becomes purely photonic because  $v_o \ll v_m$ . At such high photon energies the scattering of the phonons disappears since the corresponding refractive index is almost one. At the same time more and more partial waves will be excited, which leads to a richer angular distribution of the radiation characteristics and the possibility of Fano resonances (cf., Figs. 5 and 6 in [33]). At very large size parameters,  $ER \gg 1$ , the wavelengths will be much smaller than the radius of the quantum dot and the quasiclassical regime is entered. There, for  $E/g_0 < 1$ , the quantum dot may act as a polaritonic Veselago lens with negative refractive indices, focusing the light beam in forward direction.

### B. Oscillating quantum dot

As already mentioned above, an oscillating quantum dot causes inelastic scattering via sideband excitations  $E_n = E + n\Omega$  for both photons and the phonons. Hence, besides the angular momentum  $l$ , the sideband-energy

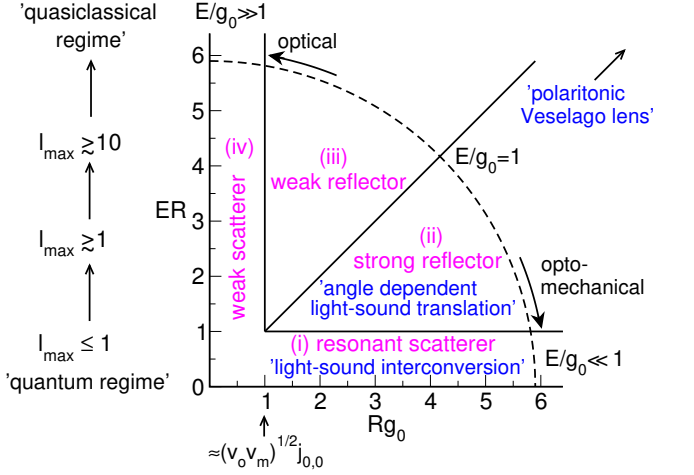


FIG. 2. (Color online) Different scattering regimes for the static quantum dot in dependence on the strength parameter  $ER$ . The latter determines the maximum angular momentum  $l_{max}$  being possible in the scattering. The energy-coupling ratio  $E/g_0$  switches between the optomechanical ( $E/g_0 \ll 1$ ) and the pure optical regime ( $E/g_0 \gg 1$ ), where the optomechanical (optical) regime is characterized by the interconversion rate  $Q^m/Q^o \sim 1$  ( $\ll 1$ ). Depending on these parameter ratios the static dot acts as a (i) resonant scatterer in the quantum regime, (ii) strong reflector, (iii) weak reflector, or (iv) weak scatterer. On the axis of abscissae the first resonance point derived from the resonance condition (15) with  $l = 0$  is marked.

quantum number  $n$  becomes important. Accordingly the scattering regimes are no longer determined by  $ER$  and  $E/g_0$ , but by effective size parameters  $E_n R$  and effective energy-coupling ratios  $E_n/g_0$ . The number of sidebands involved in the scattering is mainly determined by the ratio  $|g_1|/\Omega$ . This means, discussing the physical behavior of our setup, an additional parameter comes into play. To avoid that the sideband-excitation energies become too large and the continuum approximation is no longer justified possibly, in particular for the phonon with  $v_m \ll v_o$ , we restrict ourselves to values of  $g_0$  and  $|g_1|/2$  smaller than  $\Omega/2$ .

Before analyzing the scattering problem in detail, we want to make a general remark concerning our Floquet state approach. In the main, scattering is determined by the refractive indices, that is to say by the different wavenumbers inside and outside the scattering region. If the wavenumbers inside and outside the quantum dot are the same, scattering disappears. The other way around, strong scattering takes place for large differences between the wavenumbers belonging to the static and non-static cases. Clearly the deviation is the greater the larger the value of the coupling  $|g_1|$ . Furthermore, inspecting the quasienergies as a function of the wavenumber,  $\varepsilon(q)$ , one finds the most significant deviations close to the avoided crossings (see Fig. 12 in the Appendix). Such avoided crossings appear when two energy bands of the static case with different value of  $\tau$ , and maybe shifted by  $\Omega$ ,

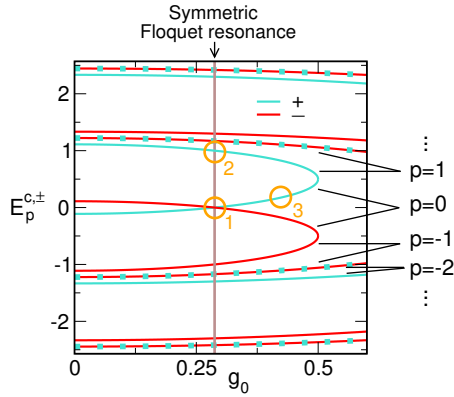


FIG. 3. (Color online) Crossing-energies (CE) according to Eq. (16). Note that in some cases CE with different  $p$  coincide (such situation is marked by points). Symmetric Floquet-resonant scattering occurs at  $g_0 = \Omega\sqrt{v_o v_m}/(v_o + v_m) \simeq 0.287\Omega$ . Circles designate particular energy-coupling ratios: (1)  $E/g_0 = 10^{-4}$  ( $E \simeq 0$ ), (2)  $E/g_0 \simeq 3.48$  ( $E = 10^{-3}g_0 + 1\Omega \simeq \Omega$ ), and (3)  $E/g_0 \simeq 0.31$  ( $E = 0.123\Omega$  at  $g_0 = 0.394\Omega$ ). They correspond to different scattering regimes of the static dot in Fig. 2: (1)  $\rightarrow$  (i), (2)  $\rightarrow$  (iii), (3)  $\rightarrow$  (ii).

cross each other. For  $g_0 \leq \Omega/2$ , these crossing-energies (CE) are:

$$E_p^{c,\pm} = \pm \frac{p'}{|p'|} \frac{\bar{v}}{\delta v} \sqrt{(p'\Omega)^2 - 4g_0^2} \pm \frac{\Omega}{4} [1 + (-1)^{p'+1}] \quad (16)$$

with  $p' = p$  for  $\pm p \geq 1$  and  $p' = p \mp 1$  for  $\pm p \leq 0$ , where  $p \in \mathbb{Z}$ . Again, the polariton degree of freedom of the CE is marked by the index  $\pm$ . Fig. 3 shows the CE depending on  $g_0$ . Since the influence of the oscillating barrier on the scattering is greatest for  $E \sim E_p^{c,\pm}$ , the further discussion follows these cases marked in Fig. 3, and the subsections are numbered accordingly.

### 1. Symmetric Floquet-resonant scattering close by $E \simeq 0$

For  $g_0 = \Omega\sqrt{v_o v_m}/(v_o + v_m)$  and an incident photon energy close to the neutrality point,  $E \simeq 0$  [case (1) in Fig. 3], the static dot is a resonant scatterer (quantum regime) which makes light-sound conversion possible [regime (i) in Fig. 2]. Since the CE with  $p = \pm 1$  are shifted by  $\pm\Omega$  with respect to the  $p = 0$  CE and the energies  $E_n$  are also shifted by multiples of  $\Omega$  amongst themselves, we call the scattering 'Floquet-resonant'. We find that different CE with  $p = 0$  cross at  $E = 0$ , which entails antiparallel wavevectors of equal magnitudes inside the dot (see Fig. 12 in the Appendix). In principle, the same argumentation applies to the sideband energies  $E_{\pm n}$ , which is why we call this situation 'symmetric'.

*a. weak photon-phonon coupling* Fig. 4 contrasts the (time-averaged) scattering efficiency of the photon and the phonon at weak couplings, i.e., in the (antiadiabatic) limit  $2|g_1| \ll \Omega$ . Obviously, the scattering efficiency of the static dot, with its resonances of the lowest

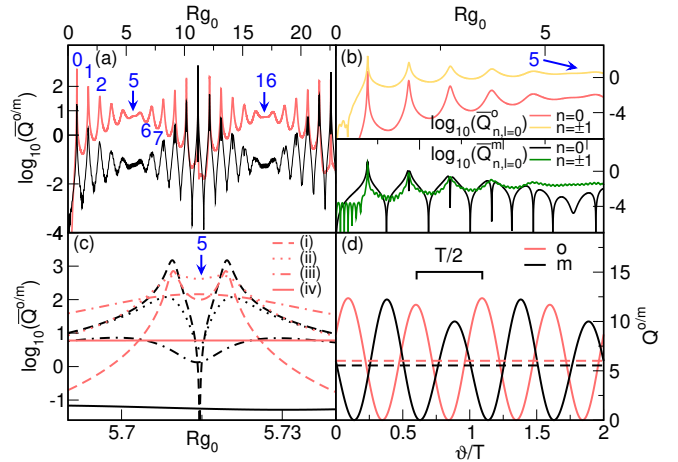


FIG. 4. (Color online) Scattering efficiency at weak coupling,  $|g_1| \ll \Omega$ . To realize symmetric Floquet resonance for  $E \simeq 0$  [case (1) in Fig. 3] we set  $E = 10^{-4}g_0 \simeq 0$ ,  $g_0 = \Omega\sqrt{v_o v_m}/(v_o + v_m) \simeq 0.287\Omega$ , and  $|g_1| = 0.02\Omega$  [except for panel (c)]. (a) Time-averaged scattering efficiency of the photon (red/grey) and the phonon (black), with resonance points  $i = 0, 1, \dots$  of the static quantum dot for  $l = 0$  according to Eq. (15) (blue numbers). (b) Different contributions to the scattering efficiency of panel (a). (c) Enlarged scattering efficiency close to  $i = 5$  for (i)  $g_1 = 0$ , (ii)  $|g_1| = 2 \cdot 10^{-3}\Omega$ , (iii)  $|g_1| = 5 \cdot 10^{-3}\Omega$ , and (iv)  $|g_1| = 0.02\Omega$ . (d) Time-averaged scattering efficiency (dashed) and time-evolution of the scattering efficiency at  $i = 5$ , corresponding to case (iv) in panel (c) (here  $Q_m$  is multiplied by a factor of 100).

partial wave  $l = 0$ , is retained to a certain extent [see panel (a)]. The resonances of the static dot can be related to minima in the scattering efficiency ( $i = 6, 7, \dots$ ). Most notably, at certain points ( $i = 5, 16, \dots$ ) the scattering is off-resonant, with the result that light-sound interconversion is strongly suppressed ( $\bar{Q}^m/\bar{Q}^o \ll 1$ ). Although not shown here, the positions of off-resonances are moving closer together, and towards smaller values of  $Rg_0$ , if  $g_1$  is increased. This can be ascribed to a Fabry-Perot interference between waves with different wavenumbers inside the dot [45].

Fig. 4 (b) gives the individual contributions to the total scattering efficiency depicted in Fig. 4 (a). Whereas in the static case the scattering is determined by the central band  $n = 0$ , for finite values of  $g_1$  the sidebands  $n = \pm 1$  are involved [sidebands with  $|n| > 1$  (not shown) play a minor role only]. Due to the symmetry of the problem for  $E \rightarrow 0$ , the  $n = \pm 1$  sideband contributions are equal in magnitude;  $|r_{n=1,l}^{o/m}| \simeq |r_{n=-1,l}^{o/m}|$ . We find that for these sidebands only the lowest partial wave with  $l = 0$  is excited, although the effective size parameter might suggest the opposite:  $E_{n=\pm 1} R \simeq \pm \Omega R \gg 1$ . We will come back to that later. We further observe that the sidebands have large impact on the scattering, even though the coupling is weak. This applies in particular to the off-resonance situation  $i = 5$ , where the scattering is dominated by the sidebands for both photons and phonons. Appar-

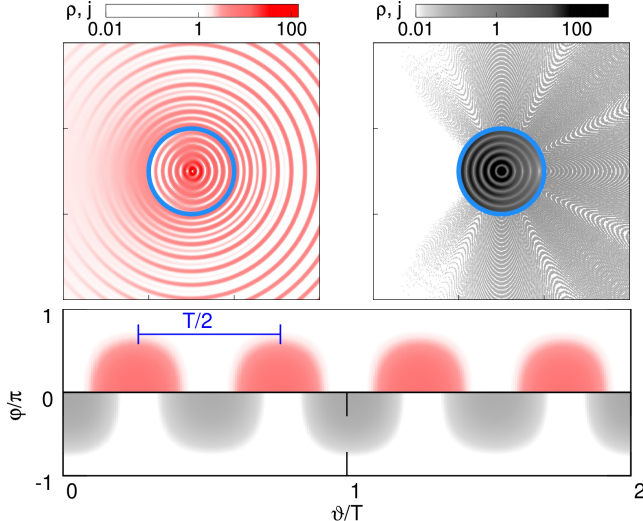


FIG. 5. (Color online) Time-retarded scattering characteristics for the same parameter values as used in Fig. 4 (d). Shown are the optical (red, top left) and mechanical (black, top right) parts of the probability density  $\rho = \langle \psi | \psi \rangle$  inside and outside the quantum dot (marked by the blue circle) at  $t = 0$ , as well as the angle-resolved time evolution of the far-field current density  $j$  according to equation (14) (bottom) at  $r = R$ . For reasons of symmetry the angle-dependence of the optical (mechanical) mode is given only for  $\varphi \geq 0$  ( $\varphi \leq 0$ ). Note that the ring structure occurring in the photon probability density also exists in the phonon density, but is hard to resolve due to the small wavelength of the phonon wave ( $v_m = v_o/10$ ) (the additional structures in the phonon density arise due to undesirable aliasing effects).

ently the occurrence of off-resonances featured by weak scattering efficiency are a direct consequence of the presence of sidebands. Since the effective energy-coupling ratio of the central band  $E_{n=0}/g_0 \simeq 0$  and the sidebands  $|E_{n=\pm 1}|/g_0 \simeq 3.48$  lie within different scattering regimes, cf. Fig. 2, their interplay may lead to a partial transition from the resonant scattering regime to the weak reflection regime [(i) to (iii) in Fig. 2], accompanied by a suppression and revival of light-sound interconversion.

To monitor how the scattering resonance of the static dot gradually dissolves and is replaced by an off-resonance, Fig. 4 (c) displays the time-averaged scattering efficiency in the vicinity of resonance point  $i = 5$  for different values of  $g_1$ . The resonance of the static dot [case (i)] is widely weakened for a small perturbation already [case (ii) and (iii)], particularly for the mechanical mode. We note that the scattering resonance is characterized by two resonance peaks, occurring symmetrically about the resonance point [33]. At even larger values of  $g_1$  the resonance almost vanishes and the scattering becomes weak and purely photonic [case (iv)].

In Fig. 4 (d) the time-dependent scattering efficiency is depicted at the off-resonance ( $i = 5$ ). According to Eq. (13), the sidebands ( $n = \pm 1$ ) interference entails a periodic time-dependence of the scattering efficiency

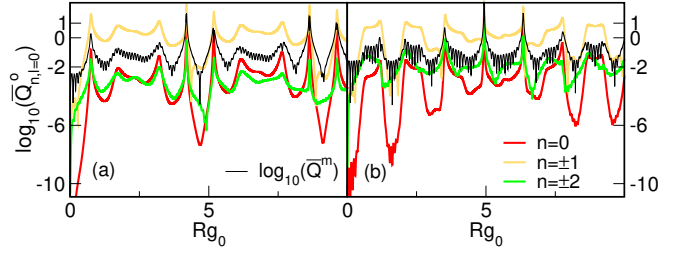


FIG. 6. (Color online) Scattering contributions  $\bar{Q}_{n,l=0}^o$  (colored/thicker lines) at moderate couplings  $|g_1| = 0.05\Omega$  (a) and  $|g_1| = 0.14\Omega$  (b). Other parameters values are the same as in Fig. 4 for the symmetric Floquet-resonant situation with  $E \simeq 0$  [case (1) in Fig. 3]. In addition, the time-averaged scattering efficiency of the phonon is depicted (black/thin line).

with frequency  $2\Omega$ . As a result the quantum dot switches between purely photonic and phononic emission. In a certain sense, this time-periodic oscillation is related to *zitterbewegung* (but see the discussion below) [41].

In Fig. 5 the time-retarded and periodic emission of light and sound by the oscillating quantum dot is illustrated by means of the probability density at  $t = 0$  (top) and the time-dependent far-field current density according to Eq. (14) at  $r = R$  (bottom) for parameters of Fig. 4 (d). The time-periodicity of the scattering efficiency displayed in Fig. 4 (d) is due to the constructive and destructive interference of the reflected wavefunctions for the sidebands  $n = \pm 1$  and gives reason to the ring structure with wavelength  $\lambda_{o/m} = \pi v_{o/m}/\Omega$  in the probability density. For the photon density the incoming wavefunction covers this periodicity farther away from the dot where the wavelength is twice as large. Inside the dot the probability density is significantly enhanced, for both photons and phonons, which can be related to the excitation of the  $l = 0$  mode [33]. Obviously, the dot captures the incident photon and partly converts it into phonons, and emits both particle waves (periodically in time) predominantly in forward direction afterwards. In the far-field, this gives rise to a time-periodic current density. The absence of backscattering at  $\varphi = \pi$ , related to Klein-tunneling, is caused by the conservation of helicity at perpendicular incidence [32, 33] and is observed for time-dependent planar barriers as well [45].

*b. moderate photon-phonon coupling* Fig. 6 shows the contributions to the time-averaged scattering efficiency of the photon in this case, where  $2|g_1| \gtrsim 0.1\Omega$ . Again only the  $l = 0$  mode is noticeably excited. We find that scattering is still dominated by the sidebands with  $n = \pm 1$ ; the contributions of the sidebands  $n = \pm 2$  are rather small and are comparable with those of the central band  $n = 0$ , see Fig. 6 (a). Sideband-contributions with  $|n| > 2$  are negligible. The situation does not change much for the relatively large coupling used in Fig. 6 (b). The minor significance of sidebands with  $|n| > 1$  is obvious by looking at the CE in Fig. 3: Since the sideband energies  $E_n = E + n\Omega \simeq n\Omega$  do not match any CE for

$n > 1$ , these sidebands become important only at very large  $g_1$ , when the influence of the closest CE is large enough. Fig. 6 furthermore shows that off-resonances are still present and get closer for the higher coupling. This is again due to interference of waves with different wavenumbers inside the dot. Hence the concomitant suppression of the light-sound interconversion at the off-resonances ( $\bar{Q}^m/\bar{Q}^o \ll 1$ ) takes place also in the weak resonant reflection regime.

*c. relation to zitterbewegung (ZB)* In a nutshell, ZB means the rapid and tiny fluctuations of the expectation value of the particle position (velocity) about the average path due to interference of positive and negative energy states. Although the effect has never been observed for a free electron due to the largeness of its rest energy, gapless metamaterials as (optomechanical) graphene with its Dirac-like quasiparticles provide a promising platform to observe ZB [41, 54–57]. Let us briefly discuss the conditions under which ZB might be observable in our setup (for the moment, we set  $v_{o/m} = 1$ ).

In absence of an oscillating barrier,  $g = 0$ , ZB may show up in the expectation value of the velocity operator  $\sigma$ . Consider a general wave packet for the optical or the mechanical mode respectively, given at  $t = 0$  as the superposition of plane wave states with positive ( $\sigma = +1$ ) and negative energy states ( $\sigma = -1$ ):  $|\psi\rangle = (1/\sqrt{2}) \sum_{\sigma} \int a^{\sigma}(k, \varphi) |\sigma, \mathbf{k}\rangle d^2\mathbf{k}$ . Here,  $a^{\sigma}(k, \varphi)$  is the probability amplitude in  $k$ -space. Straightforward calculation in the Heisenberg picture yields  $\langle v \rangle(t) = \langle v \rangle_{av} + \langle v \rangle_{ZB}(t)$  where  $\langle v \rangle_{av} = e_r \frac{1}{2} \sum_{\sigma} \sigma \int d^2\mathbf{k} |a^{\sigma}(\mathbf{k})|^2$  is the average velocity of a free, ultrarelativistic particle in polar coordinates and

$$\langle v \rangle_{ZB}(t) = -e_{\varphi} \text{Re} \left\{ \int d^2\mathbf{k} [a^+(k, \varphi)]^* a^-(k, \varphi) \times [\sin(2kt) - i \cos(2kt)] \right\} \quad (17)$$

represents the ZB term. Eq. (17) clearly shows that the interference of states with positive and negative energy is a condition for the occurrence of ZB. In addition, since the velocity operator  $\sigma$  does not act in  $k$ -space ( $\langle \sigma', \mathbf{k}' | \sigma | \sigma, \mathbf{k} \rangle \sim \delta(\mathbf{k} - \mathbf{k}')$ ), for observing ZB, states with different helicity have to be superimposed, i.e., the propagation directions of the states with positive and negative energy must be antiparallel.

Our results suggest that the setup considered here represents a realistic opportunity to observe ZB in optomechanics. Looking at the reflected wave function (5), the energetic condition for ZB can be quite simply fulfilled in the case of a symmetric Floquet resonance for photon energies at the neutrality point, see Fig. 4 (b). Here, sideband states with positive ( $E_{n=+1} \simeq +\Omega$ ) and negative ( $E_{n=-1} \simeq -\Omega$ ) energy can be symmetrically excited for both the photon and the phonon, whereby the central-band state ( $E \simeq 0$ ) fortunately is de-excited. The resulting ZB frequency of  $2\Omega$  can be made small by tuning the optomechanical coupling via the laser power ( $\Omega \sim g \sim 1\text{MHz}$  by our estimates), which should be ad-

vantageous in view of an experimental implementation, just as the simple optical readout.

We argue that the other condition can easily be fulfilled by a setup where two optomechanical barriers (circular or planar) hit by photon waves from opposite directions, generated by the probe laser after passing a beam splitter. Then, in the space between the two barriers, where the reflected waves of either barrier interfere, ZB should be able to form (this is not the case for only one barrier, where the reflected waves have same helicity). A detailed analytical and numerical analysis of a suchlike extended (much more complicated) scattering problem is beyond the scope of the present work and is therefore postponed to a forthcoming study.

## 2. Symmetric Floquet-resonant scattering close by $E \simeq \Omega$

Next we investigate the scattering of a photon with energy  $E \simeq \Omega$ , according to case (2) in Fig. 3. Since the energy-coupling ratio  $E/g_0 \simeq 3.48$ , the static quantum dot now acts as a weak reflector with almost no light-sound interconversion [regime (iii) in Fig. 2]. As before, the scattering by the oscillating dot is Floquet-resonant and the situation is, in some sense, symmetric as the energies with  $n = 0, -1, -2$  match the CE perfectly and the wavenumbers obtained from  $E_{\pm n}$  have equal magnitudes. Since  $E \neq 0$  the sideband contributions are no longer symmetric with respect to  $n \rightarrow -n$ .

In Fig. 7 the time-averaged scattering efficiency of the photon and the phonon is depicted together with the scattering contributions of the photon for two (weak) couplings ( $2|g_1| \ll \Omega$ ). The scattering is determined by the central band and the sidebands  $n = -1, -2$ ; other sidebands play no role as their energies do not lie in the range of the CE, cf. Fig. 3. For the mechanical mode only the  $n = -1$  contribution is shown because this is the only one that modifies the scattering efficiency substantially. Note that the size parameter  $ER$  takes on large values very quickly, that is why exclusively the contributions of the first partial waves were considered.

While the scattering efficiency essentially follows those of the static dot, it features some very sharp resonances, see Fig. 7 (a). The central band contribution  $n = 0$  indicates that these spikes originate from resonances of the partial waves (15) as they will also occur for a static quantum dot at zero photon energy in the resonant scattering regime. Not surprisingly, the resonant scattering regime is also reflected in the sideband contribution  $n = -1$ , where the effective energy-coupling ratio  $E_{n=-1}/g_0 \simeq 0$ . Here, only the lowest partial wave  $l = 0$  is resonant, while higher partial waves are not excited due to the smallness of the effective size parameter,  $E_{n=-1}R \ll 1$ . The situation changes for the sideband  $n = -2$ , where the effective size parameter becomes large again,  $E_{n=-2}R \gg 1$ .

Increasing the coupling strength in the weak-coupling regime, the resonances broaden [compare Figs. 7 (b) and (a)], and especially the low-frequency part in the

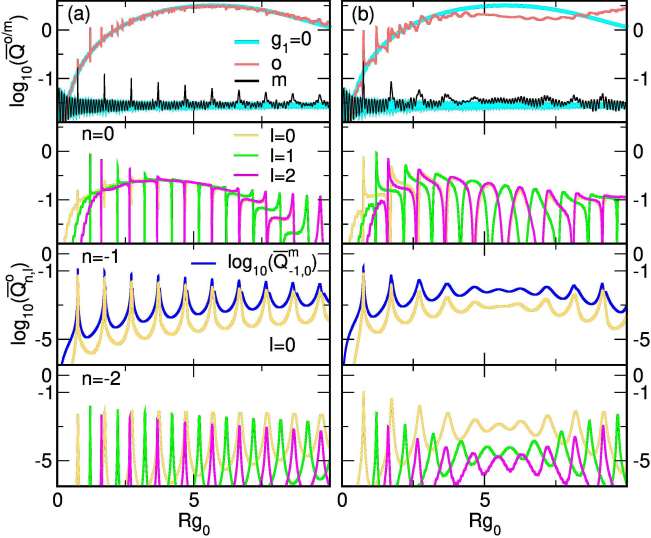


FIG. 7. (Color online) Time-averaged scattering efficiency (top panel) of the photon (red/grey) and the phonon (black) and optical scattering contributions of different partial waves (lower panels) at weak couplings, where  $|g_1| = 5 \cdot 10^{-3}\Omega$  in (a) and  $|g_1| = 0.02\Omega$  in (b). In the top panels the scattering efficiencies of the static dot are included (turquoise/thicker line). The scattering contribution of the phonon for the sideband  $n = -1$  with  $l = 0$  is denoted by the blue line. To realize a symmetric Floquet resonance at  $E \simeq \Omega$  [case (2) in Fig. 3], we choose  $E = 10^{-3}g_0 + \Omega$ ,  $g_0 = \Omega\sqrt{v_o v_m}/(v_o + v_m) \simeq 0.287\Omega$ .

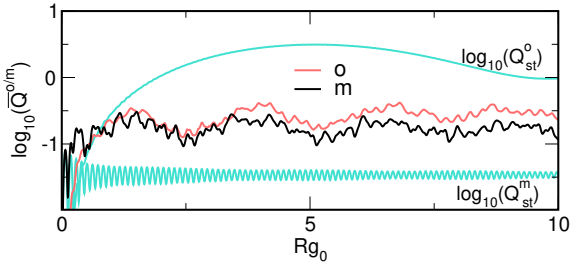


FIG. 8. (Color online) Time-averaged scattering efficiency of the photon (red/grey) and the phonon (black) slightly away from the symmetric Floquet resonance at  $E = 0.928\Omega$ ,  $g_0 = 0.3\Omega$  and  $|g_1| = 0.1\Omega$ . For comparison, the corresponding scattering efficiencies of the static dot are shown (turquoise).

functional dependence of  $\bar{Q}(Rg_0)$  markedly deviates from that of the static dot. Both effects can be attributed to larger deviations of the Floquet wavenumbers from those of the static problem when  $g_1$  is growing. Again off-resonances occur, which becomes particularly clear for the  $n = -1$  sideband contribution [see Fig. 7 (b)]. This signal is very similar to that one obtained in Fig. 4 (b), where the same value of  $g_1$  was used. The reason is that the effective energy-coupling ratio of the sideband is equal to that of a photon with energy at the neutrality point,  $E_{n=-1}/g_0 \simeq 0$ . This means that not only for  $E \simeq 0$  but also for  $E \simeq \Omega$  the interplay between sideband

and central band excitations causes a partial transition from the weak reflector regime to the resonant scattering regime [(iii) to (i) in Fig. 2], leading to the formation of a photon-dominated weak resonant scattering regime.

The scattering efficiency at moderate coupling strengths, slightly away from the symmetric Floquet resonance condition, reveals another interesting result. Figure 8 shows that in this case the scattering is no longer photon-dominated (different from Fig. 7). So while the static dot acts as a weak reflector for photons with almost no light-sound interconversion, the scattering efficiency of the phonon now becomes comparable with that in the weak scattering regime.

### 3. Floquet-resonant scattering without symmetry

Finally, we discuss the scattering by the oscillating quantum dot for a situation without symmetry. For that we assume  $E \simeq 0.12\Omega$  and  $g_0 \simeq 0.39\Omega$ , according to case (3) in Fig. 3. Then the energy-coupling ratio  $E/g_0 \simeq 0.31$ , and the static dot acts as a strong reflector with angle-dependent light-sound interconversion [regime (ii) in Fig. 2]. The scattering is again Floquet-resonant.

Figure 9 displays the time-averaged scattering efficiency of the photon and the phonon for weak and moderate coupling strength. Since the size parameter  $ER \simeq 1$ , the scattering efficiency of the static dot features resonances of the first partial waves, showing up as broad peaks. The oscillating dot weakens the resonances in the scattering efficiency of the photon as well as the light-sound interconversion rate. This effect becomes more pronounced at higher coupling strengths, and is accompanied by off-resonances for the phonon.

Figure 10 (a) gives the (relevant) photon contributions to the scattering efficiency at weak coupling. The phononic contributions are not shown because the phonon scattering efficiency is determined by the central band only. The sideband  $n = -1$  has a significant influence on the scattering efficiency as  $E_{n=-1}$  matches the CE, cf. Fig. 3. Since the corresponding effective energy-coupling ratio  $|E_{n=-1}|/g_0 \simeq 2.3$ , the interference of states of the sideband and the central band leads to the hybridization of the weak and the strong reflector regime of the static dot [regime (iii) and (ii) in Fig. 2], which gives the explanation for the weakening of resonances and of the light-sound interconversion rate in Fig. 9. We further observe, that only the first partial waves are excited for the sideband, although the effective size parameter is significantly larger,  $|E_{n=-1}|R > E_{n=0}R$ . The same effect occurs for the case of symmetric Floquet-resonant scattering at  $E \simeq 0$  in Fig. 4. It seems that the size parameter  $ER$  determines the maximum number of partial waves  $l^{max}$  which are involved in the scattering, whereas the effective size parameter  $E_{n \neq 0}R$  determines the maximum number of partial waves for the sidebands with the constraint  $l_{n \neq 0}^{max} \leq l^{max}$  (this applies also to the Floquet scattering problem in graphene [40]). This is reasonable,

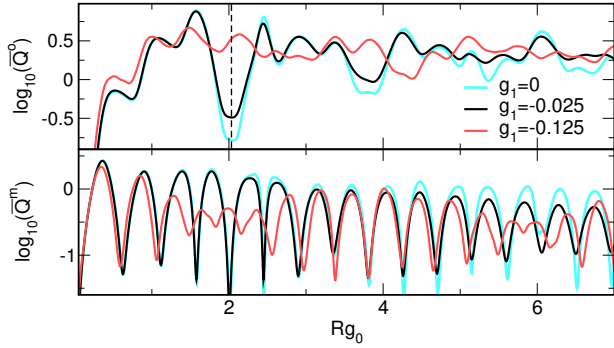


FIG. 9. (Color online) Time-averaged scattering efficiency at Floquet resonance without symmetry [case (3) in Fig. 3]. Here  $E \simeq 0.12\Omega$  and  $g_0 \simeq 0.39\Omega$ .

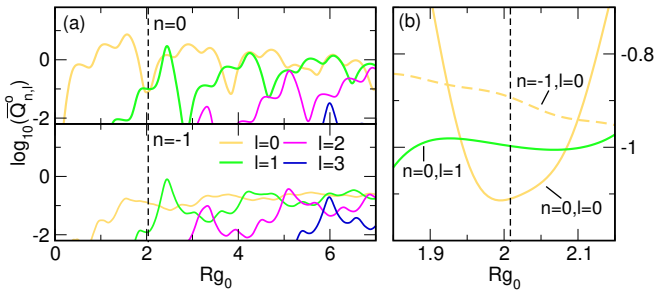


FIG. 10. (Color online) (a) Scattering contributions to  $\bar{Q}$  given in Fig. 9 for  $|g_1| = 0.025\Omega$ . (b) Enlarged area near  $Rg_0 = 2$ .

since the scattered waves with their effective size parameters merely represent the system's response, whereas the incident wave and its interaction with the quantum dot represent the initial condition of scattering.

Figure 10 (b) enlarges the area of Fig. 10 (a) where the scattering contributions of different angular momentum  $l$  and different energy  $n$  are of comparable magnitude. While the angular momentum defines the angle-dependence of the radiation, the energy determines their time-dependence, cf. Eq. (14). Interference has a lasting effect on the (angle- and time-dependent) radiation characteristics. This is illustrated in Fig. 11. At different

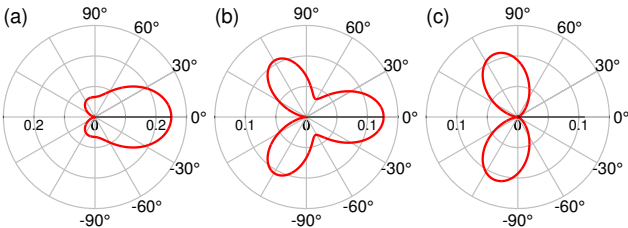


FIG. 11. (Color online) Polar plot of the current density of the optical reflected wave in the far-field according to Eq. (14) at the time  $t/2\pi = 0.61$  (a),  $t/2\pi = 1.2$  (b), and  $t/2\pi = 1.33$  (c) for  $r = R$ . Parameter values are the same as in Fig. 10 with  $Rg_0 \simeq 2$  (dashed line).

points in time the interference causes either (a) forward scattering due to the  $l = 0$  mode, (b) scattering in several directions due to the  $l = 1$  mode, or (c) the absence of forward scattering (Fano resonance) due to the interference of the  $l = 0$  and  $l = 1$  modes [33]. In this way, the oscillating quantum dot might act as a time-dependent photon transistor.

#### IV. CONCLUSIONS

The main goal of this work was to examine the time-dependent scattering of two-fold degenerate Dirac-Weyl quasiparticles by laser-driven quantum dots in optomechanical graphene. The setup considered models the propagation and interconversion of light and sound on a honeycomb array of optomechanical cells, structured by circular, oscillating (photon-phonon-coupling) barriers.

As our investigations have shown, the temporal modulation ( $\Omega$ ) of the photon-phonon coupling in the quantum dot region ( $R$ ) tremendously influences the quasiparticle transport. Here, unlike the energy-conserving case of a static quantum dot where the scattering is essentially determined by the ratio between the energy of the incident photon wave and the coupling strength of the barrier, inelastic scattering gives rise to the excitation of sideband states with energies  $E_n = E + n\hbar\Omega$ . Their interference causes a mixing of long-wavelength (quantum) and short-wavelength (quasiclassical) regimes. The number of sidebands involved is greater the larger (smaller) the amplitude (frequency) of the barrier oscillation. This affects also the effective size parameters  $E_n R$ , which determine the angular momentum contributions involved in the scattering process. The consequence is a time-periodic, strongly angle-dependent emission of light and sound (with Fano resonances), analogous to electron transport through driven graphene quantum dots. In this way, the optomechanical quantum dot acts as a time-dependent converter for photons and phonons.

Analyzing the underlying, effective two-level system within Floquet theory, it was shown that avoided crossings in the quasienergy bandstructure are of particular importance. More specifically, when the (sideband) energy lies in the vicinity of an avoided crossing (Floquet resonance), the influence of the barrier is most prominent since the wavenumbers determining the scattering process most deviate from those of the static dot. Then even a small oscillation amplitude may significantly affect the scattering, up to the point where the light-sound interconversion is suppressed and revived in the course of interference of waves with different wavenumbers.

The results presented in this work should have impact on both, fundamental problems such as the observation of *zitterbewegung* and potential applications based on quantum-optical, laser/field-driven optomechanical metamaterials being suitable for the transport, storage and transduction of photons and phonons. In this context, a more realistic description of optomechanical sys-

tems beyond the continuum approximation, which ideally involves wave packet dynamics and dissipation, is highly desirable, as well as more in-depth studies about the role of time-dependent (synthetically generated) magnetic fields [31].

## ACKNOWLEDGMENTS

The authors would like to thank K. Rasek for valuable discussions.

## Appendix: Implementation of the Floquet approach

Inserting the Floquet state (3) into the time-dependent Dirac equation yields the Floquet eigenvalue equation

$$\begin{aligned} & \sum_p \sum_{\tau=\pm} \left\{ c_p^\tau (E^{\tau,\sigma} + p\Omega) |\tau\rangle \delta_{pp'} \right. \\ & \left. + g_1 \sum_{\tau'=\pm} c_p^\tau \alpha_{\tau'}^\tau |\tau'\rangle (\delta_{p+1,p'} + \delta_{p-1,p'}) \right\} \\ & = \varepsilon \sum_p \sum_{\tau=\pm} c_p^\tau |\tau\rangle \delta_{pp'}, \quad p' \in \mathbb{Z}, \end{aligned} \quad (\text{A.1})$$

where

$$E^\tau = \bar{v}\sigma q + \sigma\tau \sqrt{g_0^2 + \delta v^2 q^2/4} \quad (\text{A.2})$$

is the energy dispersion of the time-independent problem for wavenumber  $q$ , and

$$\alpha_+^\tau = \frac{\mathcal{N}^\tau}{\mathcal{N}^+} \frac{g_0^2 - \gamma^\tau \gamma^+}{g_0 (\gamma^+ - \gamma^-)} = -\tau \alpha_-^{-\tau} \quad (\text{A.3})$$

with the normalization factor

$$\mathcal{N}^\tau = 1/\sqrt{g_0^2 + (\gamma^\tau)^2}, \quad \gamma^\tau = v_o\sigma q - E^\tau. \quad (\text{A.4})$$

Based on Eq. (A.1) we define the vector of Fourier components,  $\mathbf{c} = (\dots, c_{-1}^+, c_{-1}^-, c_0^+, c_0^-, c_1^+, c_1^-, \dots)^T$ , and the (Hermitian) Floquet matrix

$$\mathcal{F} = \begin{pmatrix} \ddots & & & & & & \\ & E_{-1}^+ & 0 & g_1 \alpha_+^+ & g_1 \alpha_-^- & 0 & 0 \\ & 0 & E_{-1}^- & g_1 \alpha_+^- & g_1 \alpha_-^+ & 0 & 0 \\ g_1 \alpha_+^+ & g_1 \alpha_-^- & E^+ & 0 & g_1 \alpha_+^+ & g_1 \alpha_-^- & \\ g_1 \alpha_-^- & g_1 \alpha_+^+ & 0 & E^- & g_1 \alpha_+^- & g_1 \alpha_-^+ & \\ 0 & 0 & g_1 \alpha_+^+ & g_1 \alpha_-^- & E_{+1}^+ & 0 & \\ 0 & 0 & g_1 \alpha_-^- & g_1 \alpha_+^+ & 0 & E_{+1}^- & \ddots \end{pmatrix} \quad (\text{A.5})$$

for  $E_n^\tau = E^\tau + n\Omega$ . We fix  $\Omega = 1$ , which is justified due to the scale invariance of the scattering problem. The quasienergies  $\varepsilon$  in  $\mathcal{F}\mathbf{c} = \varepsilon\mathbf{c}$  are obtained as the eigenvalues of the Floquet matrix (A.5) and depend on the

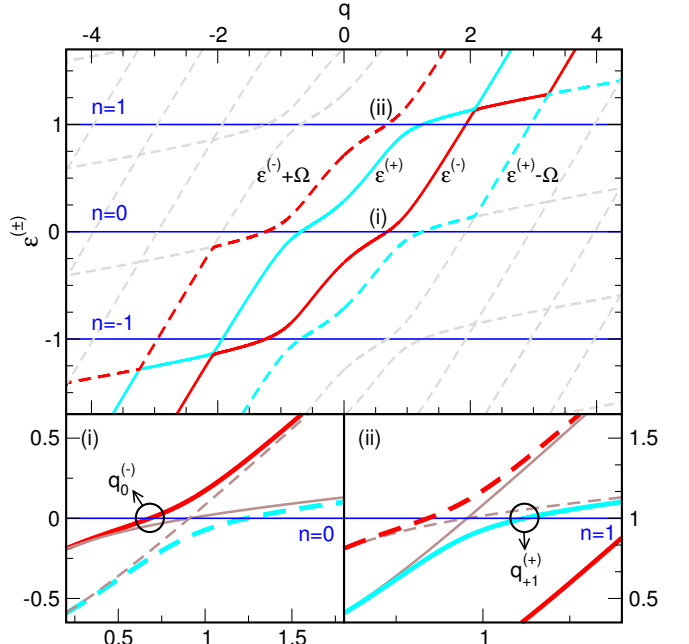


FIG. 12. (Color online) Quasienergies  $\varepsilon^{(\pm)} + n\Omega$ ,  $n \in \mathbb{Z}$ , obtained as eigenvalues of the Floquet matrix (A.5) for  $|g_1| = 0.14\Omega$  as a function of the wavenumber  $q$  (using  $\sigma = \pm 1$  for positive/negative values of  $q$ ). Inserted are also the energies  $E_n = E + n\Omega$  of the central band  $n = 0$  and the sidebands  $n = \pm 1$  (blue horizontal lines) for  $E = 0$  and static coupling  $g_0 = 0.287\Omega$ , corresponding to the case of symmetric Floquet resonance close by  $E \simeq 0$  (see discussion in Sec. III B 1 of the main text). The proper pair of quasienergies  $\varepsilon^{(\pm)}$  (solid lines) that has to be used for the scattering problem is that which coincides with the dispersion of the static case at  $q \rightarrow 0$ . The wavenumbers used for the scattering problem are determined by the zeros of  $E_n - \varepsilon^{(\pm)}(q)$  and are marked exemplary for the cases  $n = 0, 1$  in the lower panels (i) and (ii). For comparison the polariton branches of the energy dispersion of the static case,  $E^\pm(q)$  (solid) and  $E^\pm(q) \mp \Omega$  (dashed), are shown (brown thin lines). Since  $E = 0$ , the wavenumbers reveal the symmetry  $q_{-n}^{(\pm)} = -q_n^{(\mp)}$ .

two barrier parameters  $g_0, g_1$ , as well as on wavenumber  $q$ . The pseudospin projection  $\sigma = \pm 1$  leads only to a change in the sign of the quasienergies and is determined by the sign of the wavenumber. As a consequence of the polariton degree of freedom  $\tau = \pm 1$ , the static dispersion (A.2) is two-fold degenerate. Accordingly, the quasienergies are two-fold degenerate too, which is reflected in the block-diagonal form of  $\mathcal{F}$  and is marked by the index  $(\pm)$  hereinafter. Diagonalization yields a pair of quasienergies  $\varepsilon^{(\pm)}(q)$  with Fourier vectors  $\mathbf{c}^{(\pm)}(q)$  for each  $q$ . Other pairs of quasienergies  $\varepsilon^{(\pm)}(q) + n\Omega$  are also eigensolutions of Eq. (A.5), but in principle they all contain the same information about the time-dependence.

According to Eq. (6), the eigensolutions of  $\mathcal{F}$  are needed to construct the transmitted wavefunction inside the dot. Since the oscillating barrier shifts the energy  $E$  of the incoming wave,  $E_n = E + n\Omega$ , the quasienergies are

fixed:  $\varepsilon^{(\pm)}(q) = E_n$ . The zeros of  $\varepsilon^{(\pm)}(q) - E_n$  yield the wavenumbers  $q_n^{(\pm)}$ , and hence the Fourier vectors  $\mathbf{c}_n^{(\pm)}$  can be calculated. Doing this it makes sense to connect the considered pair of quasienergies with the energy dispersion in the static case for  $q \rightarrow 0$ :  $\varepsilon^{(\pm)}(q \rightarrow 0) = E^{\pm}(q \rightarrow 0)$ . We note that when using the Floquet approach the specific geometry of the barrier only enters the scattering matrix via Eqs. (8) and (9) (e.g., the results for a planar barrier are given in [45]).

Fig. 12 displays the highly symmetric situation that evolves in the numerical work for the Floquet resonance at photon energy  $E \simeq 0$  discussed in the main text. By tracking the quasienergies in dependence of  $q$ , the condition  $\varepsilon^{(\pm)}(q) = E_n$  defines the wavenumbers  $q_n^{(\pm)}$  (and Fourier vectors) that have to be used for the barrier wavefunction (crossings of the blue horizontal lines with the quasienergies), see panels (i) and (ii) for  $n = 0, 1$ . Deviations of the wavenumbers  $q$  from those of the dispersion of the static case (obtained from crossings of the horizontal lines with the brown thin lines in lower panels of

Fig. 12) arise due to the avoided crossings. Obviously, these deviations are largest in the vicinity of the points where the two polariton branches of the static dispersion cross each other. The corresponding crossing-energies (CE) are given by Eq. (16). Of course, the influence of the oscillating barrier on the scattering is most prominent for energies  $E_n$  near a CE. There even small couplings  $|g_1| \ll \Omega$  significantly modify the scattering, cf. Fig. 3, Fig. 6, and Fig. 8.

We finally note that at larger  $|q|$  values the quasienergies are less affected by the barrier; for  $|q| \gg 1$  the quasienergy and the dispersion of free quasiparticles merge. This can be used to implement a truncation criteria for the number of sidebands  $n_{max}$  which will have to be considered in the numerical work. Taking into account that  $2|g_1| \leq g_0$ , we found that  $\dim \mathcal{F} \simeq 2 + 4(x-1)$  with  $x = 2(1 + 10 \cdot 4|g_1|)$  serves as a good estimate for numerical convergence of the quasienergies  $\varepsilon^{(\pm)}$  as well as for those of the scattering coefficients. Then the maximum number of sidebands used in the numerics should be at least  $n_{max} = x/2$ , i.e.,  $n_{max} \simeq 1 + 10 \cdot 4|g_1|$ .

---

[1] M. Aspelmeyer, T. J. Kippenberg, and F. Marquardt, Rev. Mod. Phys. **86**, 1391 (2014).

[2] J. Chan, T. P. M. Alegre, A. H. Safavi-Naeini, J. T. Hill, A. Krause, S. Gröblacher, M. Aspelmeyer, and O. Painter, Nature **478**, 89 (2011).

[3] J. D. Teufel, T. Donner, D. Li, J. W. Harlow, M. S. Allman, K. Cicak, A. J. Sirois, J. D. Whittaker, K. W. Lehnert, and R. W. Simmonds, Nature **495**, 359 (2011).

[4] M. Frimmer, J. Gieseler, and L. Novotny, Phys. Rev. Lett. **117**, 163601 (2016).

[5] F. Marquardt, J. G. E. Harris, and S. M. Girvin, Physical Review Letters **96**, 103901 (2006).

[6] C. Wurl, A. Alvermann, and H. Fehske, Phys. Rev. A **94**, 063860 (2016).

[7] L. Bakemeier, A. Alvermann, and H. Fehske, Phys. Rev. Lett. **114**, 013601 (2015).

[8] J. Qian, A. A. Clerk, K. Hammerer, and F. Marquardt, Phys. Rev. Lett. **109**, 253601 (2012).

[9] C. Schulz, A. Alvermann, L. Bakemeier, and H. Fehske, Europhys. Lett. **113**, 64002 (2016).

[10] D. Vitali, S. Gigan, A. Ferreira, H. R. Böhm, P. Tombesi, A. Guerreiro, V. Vedral, A. Zeilinger, and M. Aspelmeyer, Phys. Rev. Lett. **98**, 030405 (2007).

[11] R. Ghobadi, S. Kumar, B. Pepper, D. Bouwmeester, A. I. Lvovsky, and C. Simon, Phys. Rev. Lett. **112**, 080503 (2014).

[12] Y.-D. Wang and A. A. Clerk, Phys. Rev. Lett. **108**, 153603 (2012).

[13] J. T. Hill, A. H. Safavi-Naeini, J. Chan, and O. Painter, Nature Communications **3**, 1196 (2012), article.

[14] T. A. Palomaki, J. W. Harlow, J. D. Teufel, R. W. Simmonds, and K. W. Lehnert, Nature **475**, 210 (2013).

[15] M. J. Weaver, F. Buters, F. Luna, H. Eerkens, K. Heeck, S. de Man, and D. Bouwmeester, Nature Communications **8**, 824 (2017).

[16] M. Eichenfield, J. Chan, R. M. Camacho, K. J. Vahala, and O. Painter, Nature **462**, 78 (2009).

[17] A. H. Safavi-Naeini and O. Painter, Opt. Express **18**, 14926 (2010).

[18] A. H. Safavi-Naeini, T. P. M. Alegre, M. Winger, and O. Painter, Applied Physics Letters **97**, 181106 (2010).

[19] A. H. Safavi-Naeini, J. T. Hill, S. Meenehan, J. Chan, S. Gröblacher, and O. Painter, Phys. Rev. Lett. **112**, 153603 (2014).

[20] G. Heinrich, M. Ludwig, J. Qian, B. Kubala, and F. Marquardt, Phys. Rev. Lett. **107**, 043603 (2011).

[21] A. Xuereb, C. Genes, and A. Dantan, Phys. Rev. Lett. **109**, 223601 (2012).

[22] M. Ludwig and F. Marquardt, Phys. Rev. Lett. **111**, 073603 (2013).

[23] D. E. Chang, A. H. Safavi-Naeini, M. Hafezi, and O. Painter, New Journal of Physics **13**, 023003 (2011).

[24] A. H. Safavi-Naeini and O. Painter, New Journal of Physics **13**, 013017 (2011).

[25] M. Schmidt, M. Ludwig, and F. Marquardt, New Journal of Physics **14**, 125005 (2012).

[26] W. Chen and A. A. Clerk, Phys. Rev. A **89**, 033854 (2014).

[27] K. Fang, M. H. Matheny, X. Luan, and O. Painter, Nature Photonics **10**, 489 (2016).

[28] M. Schmidt, S. Kessler, V. Peano, O. Painter, and F. Marquardt, Optica **2**, 635 (2015).

[29] S. Walter and F. Marquardt, New Journal of Physics **18**, 113029 (2016).

[30] M. Aidelsburger, S. Nascimbene, and N. Goldman, arXiv:1710.00851v1 [cond-mat.mes-hall] (2017).

[31] V. Peano, C. Brendel, M. Schmidt, and F. Marquardt, Phys. Rev. X **5**, 031011 (2015).

[32] M. Schmidt, V. Peano, and F. Marquardt, New Journal of Physics **17**, 023025 (2015).

[33] C. Wurl and H. Fehske, Scientific Reports **7**, 9811 (2017).

[34] G. Platero and R. Aguado, Physics Reports **395**, 1 (2004).

[35] M. V. Fistul and K. B. Efetov, Phys. Rev. Lett. **98**,

256803 (2007).

[36] M. A. Zeb, K. Sabeeh, and M. Tahir, *Phys. Rev. B* **78**, 165420 (2008).

[37] W.-T. Lu, S.-J. Wang, W. Li, Y.-L. Wang, C.-Z. Ye, and H. Jiang, *Journal of Applied Physics* **111**, 103717-103717-4 (2012).

[38] C. Sinha and R. Biswas, *Applied Physics Letters* **100**, 183107 (2012).

[39] R. Biswas and C. Sinha, *Journal of Applied Physics* **114**, 183706 (2013).

[40] C. Schulz, R. L. Heinisch, and H. Fehske, *Phys. Rev. B* **91**, 045130 (2015).

[41] B. Trauzettel, Y. M. Blanter, and A. F. Morpurgo, *Phys. Rev. B* **75**, 035305 (2007).

[42] J. H. Shirley, *Phys. Rev.* **138**, B979 (1965).

[43] S.-K. Son, S. Han, and S.-I. Chu, *Phys. Rev. A* **79**, 032301 (2009).

[44] T. Bilitewski and N. R. Cooper, *Phys. Rev. A* **91**, 033601 (2015).

[45] C. Wurl and H. Fehske, *Proceedings FQMT 2017 Prague*.

[46] P. Rakich and F. Marquardt, *New Journal of Physics* **20**, 045005 (2018).

[47] M. Grifoni and P. Hänggi, *Physics Reports* **304**, 229 (1998).

[48] S.-I. Chu and D. A. Telnov, *Physics Reports* **390**, 1 (2004).

[49] C. Deng, F. Shen, S. Ashhab, and A. Lupascu, *Phys. Rev. A* **94**, 032323 (2016).

[50] G. Floquet, *Annales scientifiques de l'École Normale Supérieure* **12**, 47 (1883).

[51] R. L. Heinisch, F. X. Bronold, and H. Fehske, *Phys. Rev. B* **87**, 155409 (2013).

[52] C. Schulz, R. L. Heinisch, and H. Fehske, *Quantum Matter* **4**, 346 (2015).

[53] J.-S. Wu and M. M. Fogler, *Phys. Rev. B* **90**, 235402 (2014).

[54] M. I. Katsnelson, *Eur. Phys. J. B* **51**, 157 (2006).

[55] J. C. Martinez, M. B. A. Jalil, and S. G. Tan, *Applied Physics Letters* **97**, 062111 (2010).

[56] W. Zawadzki and T. M. Rusin, *Journal of Physics: Condensed Matter* **23**, 143201 (2011).

[57] T. García, N. A. Cordero, and E. Romera, *Phys. Rev. B* **89**, 075416 (2014).